DELIVERABLE REPORT

Deliverable no. / title:	4.2 / Simplified Model of the Electrochemical Double Layer
Lead beneficiary:	ZHAW - Institute of Computational Physics
Nature of deliverable:	Report
Dissemination level:	Public
Due date:	M30 / June 2022
Grant Agreement number:	**875489**
Project acronym:	**SONAR**
Project title:	**Modelling for the search for new active materials for redox flow batteries**
Funding scheme:	**H2020-LC-BAT-2019**
Coordinator:	Fraunhofer ICT Jens Noack **Tel:** 0049 721 4640 870 **E-mail:** jens.noack@ict.fraunhofer.de
Project website:	www.sonar-redox.eu
Disclaimer:	This project has received funding from the European Union's Horizon 2020 research and innovation programme under Grant Agreement no. 875489. This report reflects only the authors' view. The funding agency is not responsible for any use made of the information it contains.

Table of contents

1 Introduction

Redox flow batteries are a promising emerging technology for the storage of intermittent energy sources. The energy conversion between electrical energy and chemical energy via heterogeneous electrochemical redox reactions at the electrode interface is a critical process affecting both the efficiency and lifetime of the battery. Generally, the charge transfer at the electrode surface depends on various geometrical, physical and chemical properties, such as the electrode surface morphology, chemical surface composition and operating conditions, such as temperature, pressure and species concentrations.

The interactions of the electrolyte species with the electrode surface and the resulting presence of a strong electric field leads to the formation of a characteristic electrochemical double layer structure. It is well-known that theories based on the Poisson-Boltzmann equation,

such as the Gouy-Chapman model, only allow for realistic double layer predictions within a very limited voltage range, as the assumption of point charges leads to unrealistic predictions of species concentrations within the double layer [1]. Several modifications of the Poisson-Boltzmann equation have been considered, where, among other properties, the steric effect of the finite sized ions is taken into consideration [1, 2, 13, 14, 17, 20].

In contrast to this simplified mean field theory, atomistic simulations of the electrochemical interface, such as DFT [8, 19] and KMC simulations [18], allow for very detailed investigations of interface properties and processes. However, due to the high computational demands of such atomistic simulations, comprehensive parameter studies would require tremendous computational resources.

In a series of papers, Dreyer, Guhlke, Landstorfer, and Müller published a treatment of the electrochemical double layer based on non-equilibrium thermodynamics [4, 5, 6, 12], which we refer to as the DGLM-theory in the following. This model allows for the prediction of reaction rates, adsorption processes and the electrochemical double layer structure. The reduced nature of the model allows very fast evaluations, enabling large parameter or sensitivity studies.

A full parameterization of the DGLM-model requires in-depth knowledge about the involved electrolyte species and properties of the double layer. While some model parameters, such as the adsorption rates, can be parameterized directly by DFT calculations provided by WP3, other parameters can be inferred indirectly by updating the model parameters to decrease the error between model predictions and atomistic simulations or measurements of some target variable.

Here we propose a work flow based on a statistical approach, where the model input parameters are modelled as statistical distribution functions, allowing for the incorporation of uncertainties in the parameters. We use Bayesian inference methods to update the initial model parameters based on measurement data or atomistic simulations, such as KMC and DFT, which allows establishing a natural interface to the results of WP2 and WP3 in the SONAR project.

We implemented the DGLM-theory as a Julia package that allows performing Bayesian inference to update the model parameters. In this report we present various verification and validation studies of the model, together with applications to two relevant all-organic electrolyte systems used for RFB applications.

2 Reduced Electrochemical Double Layer Model

In this section we discuss the main modelling assumptions of the reduced electrochemical double layer model, present some key results of the DGLM-thoery, and describe the Bayesian inference methods used to update the model parameters.

2.1 Thin Double Layer Approximation

A characteristic length scale l^0 of the double layer thickness is provided by the Debye length, which for electrolyte solutions is given by

$$\lambda_D = \left(\frac{\varepsilon_0 \varepsilon_r RT}{2F^2 I} \right)^{1/2}, \quad I = \frac{1}{2} \sum_\alpha z_\alpha c_\alpha, \tag{1}$$

where $\varepsilon_0, \varepsilon_r$ denote the permittivity of free space and the dielectric constant of the electrolyte, respectively. Furthermore, I denotes the ionic strength of the electrolyte.

In RFB applications, the electrode is typically a porous material through which the liquid electrolyte is forced by an applied pressure difference. For transport simulations at the pore-scale, a characteristic length scale L^0 is given by the mean pore diameter, which is in the range of 10-100 µm for typical electrode materials, see [9]. In contrast, evaluating the Debye length in Eq. (1) for a symmetric 1:1 electrolyte at a concentration of $1\,\mathrm{M}$ yields a Debye length on the order of only $1\,\mathrm{nm}$. Thus, the thickness of the double layer can be considered negligible compared to the relevant length scale in pore-scale simulations. Formally, we can define the dimensionless Debye length $\bar{\lambda}_D = l^0/L^0$, which we consider to be much smaller than one. This scale separation allows for a significant simplification of the mathematical description of the interface properties by means of an asymptotic expansion in terms of the dimensionless scale parameter $\bar{\lambda}_D$, see e.g. [6, 7].

Furthermore, for electrode felt materials consisting of cylindrical carbon fibers with a characteristic diameter given by $L_d^0 = 10\,\mu\mathrm{m}$, the electrode surface is locally well-approximated by a flat surface when considering surface areas on the order of λ_D^2. As such, mean surface curvature effects on the double layer structure can be neglected in this case. Thus, the electrode-electrolyte interface region can be reduced to a one-dimensional domain in the direction orthogonal to the electrode surface.

In addition to the spatial scale separation, we assume the characteristic timescale of the interfacial relaxation processes within the double layer structure to be much shorter than the timescale of variations in the boundary conditions. This simplifying assumption allows to describe the double layer structure to be in a quasi-equilibrium state. Clearly, this restricts the applicability of the model to temporal processes that vary slowly (e.g. on the order of seconds), compared to the processes within the double layer, such as adsorption processes.

Figure 1 shows a visualization of the electrostatic potential, which varies smoothly through the fully resolved double layer structure at the nanometer scale. In the limiting case of $\bar{\lambda}_D \to 0$, the double layer structure can be described as an interface with jump conditions for the field variables.

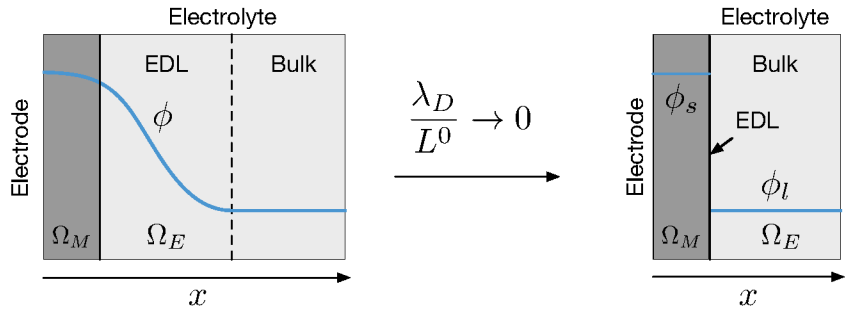

Figure 1: Visualization of the double layer structure (left) and the simplified description in the limit of $\bar{\lambda}_D \to 0$ (right). The electrochemical interface domain consists of a solid electrode domain Ω_M and an electrolyte domain Ω_E.

2.2 Extended Butler-Volmer Model

In the publications [4, 6] an asymptotic expansion of the transport equations in terms of a small interface thickness $\bar{\lambda}_D$ was carried out. As a result two models for the thin double layer approximation were derived: A reduced interface model based on the leading order approximation of the bulk transport equations and a boundary layer model based on the inner asymptotic expansion, which describes the resolved double layer structure in detail. It was found that these two models are only weakly coupled through the interface electroneutrality condition.

We denote the species present in either the electrode, electrolyte or electrode surface as $\mathscr{A} = \{A_0, \ldots, A_N\}$, where A_0 refers to the solvent. For simplicity we consider in the following reactions, where no surface-exclusive species exist, i.e. all species present on the electrode surface also exist either in the electrolyte or the electrode domain. The more general case with exclusive surface species is presented in [4].

Let us first consider the general surface reactions

$$\underset{s}{a^i_0} A_0 + \ldots \underset{s}{a^i_N} A_N \rightleftharpoons \underset{s}{b^i_0} A_0 + \ldots \underset{s}{b^i_N} A_N, \quad i = 1, \ldots, M_s, \tag{2}$$

where the coefficients $\underset{s}{a^i_\alpha}, \underset{s}{b^i_\alpha}$ denote non-negative integers, so that $\underset{s}{\gamma^i_\alpha} = \underset{s}{b^i_\alpha} - \underset{s}{a^i_\alpha}$ is the stoichiometric coefficient of species α in reaction i. The corresponding Faradaic current density reads

$$j_e \nu|_I = -F \sum_{i=1}^{M_S} \underset{s}{R^i} \underset{s}{\gamma^i_e}, \tag{3}$$

where $\underset{s}{R^i}$ is the reaction rate of the i-th reaction, I denotes the electrochemical interface and ν is the unit normal vector pointing from the electrolyte domain Ω_E into the electrode domain Ω_M.

Let $\Delta\phi = \phi_E - \phi_M$ denote the electrostatic potential difference between the electrolyte bulk and the metal bulk regions. Analogously, $\Delta\bar{\phi} = \bar{\phi}_E - \bar{\phi}_M$ is the electrostatic potential difference

under equilibrium conditions. For a general (electro-)chemical surface reaction of the form (2), the reaction rate satisfies the extended Butler-Volmer type equation [4]

$$R_s^i = R_f^{0,i} \exp\left(-\alpha_f^i f \eta_s\right) - R_b^{0,i}\left(\alpha_b^i f \eta_s\right) \tag{4}$$

with the transfer coefficients

$$\alpha_f^i = \beta_s^i A_s^i \Gamma_+^i \quad \text{and} \quad \alpha_b^i = (1-\beta_s^i) A_s^i \Gamma_+^i \quad \text{with} \quad \Gamma_+^i = \sum_{\mathscr{A}_E} \gamma_{\alpha s}^i z_\alpha, \tag{5}$$

where $\mathscr{A}_E$ represents all species present in the electrolyte domain. Furthermore, $\eta_s = \Delta\phi - \Delta\bar{\phi}$ denotes the applied overpotential and

$$R_f^{0,i} = R_{0s}^i \exp\left(-\beta_s^i f A_s^i h\right), \quad R_b^{0,i} = R_{0s}^i \exp\left((1-\beta_s^i) f A_s^i h\right) \quad \text{with} \quad h = \sum_\alpha \gamma_{\alpha s}^i (\mu_\alpha - \bar{\mu}_\alpha)|_I \tag{6}$$

are the forward and backward reaction rates, respectively, where

$$\mu_\alpha = \mu_\alpha^0 + RT \ln(\gamma_\alpha) \quad \text{with} \quad y_\alpha = \frac{c_\alpha}{\sum_\beta c_\beta} \tag{7}$$

denotes the chemical potential of species α. Analogously, $\bar{\mu}_\alpha$ is the chemical potential at the equilibrium state. The coefficients R_{0s}^i, β_s^i, A_s^i denote phenomenological coefficients satisfying

$$R_{0s}^i \geq 0, \quad 0 \leq \beta_s^i \leq 1, \quad A_s^i \geq 0, \tag{8}$$

for the resulting entropy production of the system to be non-negative.

Specializing this generalized form of the Butler-Volmer equation to a redox reaction

$$\mathscr{A}_{\mathrm{ox}s} + n e^- \rightleftharpoons \mathscr{A}_{\mathrm{red}s} \tag{9}$$

yields the simplified equation [4]

$$R_s = R_{0s}\left[\left(\frac{\bar{y}_{\mathrm{red}}}{\bar{y}_{\mathrm{ox}}}\frac{y_{\mathrm{ox}}}{y_{\mathrm{red}}}\right)^{\beta_s A_s} \exp\left(-\beta_s A_s n f \eta_s\right) - \left(\frac{\bar{y}_{\mathrm{ox}}}{\bar{y}_{\mathrm{red}}}\frac{y_{\mathrm{red}}}{y_{\mathrm{ox}}}\right)^{(1-\beta_s)A_s} \exp\left((1-\beta_s) A_s n f \eta_s\right)\right]. \tag{10}$$

For a single n-electron redox reaction, the resulting Faradaic current density at the electrode interface is then given by

$$j_e^F \nu|_I = nF \sum_s R_s. \tag{11}$$

2.3 Total Current Density

Generally, the total electric current density at an electrode-electrolyte interface can be decomposed into a Faradaic current j_e^F and a non-Faradaic current j_e^P, so that

$$j_e = j_e^F + j_e^P. \tag{12}$$

In case of a single redox reaction the Faradaic contribution can be written as

$$j_e^F = nF\underset{s}{R}, \tag{13}$$

where $\underset{s}{R}$ denotes the reaction rate. Additionally, charging and adsorption processes in the double layer give rise to a non-Faradaic current. Let σ denote the surface charge density on the electrode, then

$$j_e^P = -\frac{d\sigma}{dt} = -\frac{d\sigma}{d\Delta\phi}\frac{d\Delta\phi}{dt} = C\frac{d\Delta\phi}{dt}, \tag{14}$$

where C denotes the differential capacitance of the double layer structure defined as

$$C \equiv \frac{dq}{d\Delta\phi}, \tag{15}$$

where q denotes the total charge stored in the double layer structure.

2.4 Double Layer Structure

To evaluate the non-Faradaic current density, we need to model the total charge q stored in the double layer structure in terms of the potential difference $\Delta\phi$ across the double layer. In the following we present a short summary of the double layer model presented in [12].

The spatial extent of each species is considered by its partial molar volume ν_α in the electrolyte at a fixed reference state. The solvation shells of the charged species are taken explicitly into account by considering their impact on the effective size of the ions as

$$\nu_\alpha = \tilde{\nu}_\alpha + \kappa_\alpha \nu_0, \tag{16}$$

where $\tilde{\nu}_\alpha$ is the partial molar volume of the central charged ion, κ_α is the solvation shell number of species α and ν_0 denotes the partial molar volume of the solvent.

Let $c = \sum_\alpha c_\alpha$ denote the total species concentration in the electrolyte. As the electrolyte is

modelled as an incompressible fluid, the volumetric constrained

$$c\sum_{\alpha} \nu_\alpha y_\alpha = 1 \tag{17}$$

must be satisfied.

As shown in [12], the molar fraction of species α satisfies

$$y_\alpha = y_{E,\alpha} \exp\left(-z_\alpha f(\phi - \phi_E) - \frac{\nu_\alpha}{RT}(p - p_E)\right), \tag{18}$$

in the double layer structure, where $y_{E,\alpha}, \phi_E, p_E$ denote the molar fraction, potential and pressure evaluated in the electrolyte bulk domain.

The pressure p in Eq. (18) can be evaluated for a given electrostatic potential ϕ by solving the constraint equation

$$\sum_{\alpha} \hat{y}_\alpha(\phi, p) = 1. \tag{19}$$

Let q_{BL} denote the total charge stored in the electrolyte within the double layer structur (excluding the surface charge). Landstorfer shows in [12] the important relation

$$q_{\mathrm{BL}} = -\sigma = \mathrm{sgn}(\Delta\phi)\sqrt{2(1+\chi)\varepsilon_0 \Delta p}, \tag{20}$$

so that the charge stored in the boundary layer can be evaluated directly from the potential and pressure differences through the double layer.

The differential capacitance of the boundary layer can be evaluated explicitly from given potential and pressure differences as

$$C_{\mathrm{BL}}(\Delta\phi_{\mathrm{DL}}, \Delta p_{\mathrm{DL}}) = \frac{\sqrt{\varepsilon_0(1+\chi)}\,\mathrm{sgn}(\Delta\phi_{\mathrm{DL}})}{\sqrt{2\Delta p_{\mathrm{DL}}}} \frac{\partial p}{\partial \phi}(\Delta\phi_{\mathrm{DL}}, \Delta p_{\mathrm{DL}}) \quad \text{with} \quad \frac{\partial p}{\partial \phi} = -F\frac{\sum_\alpha z_\alpha y_\alpha}{\sum_\alpha \nu_\alpha y_\alpha}. \tag{21}$$

2.5 Surface Coverage by Adsorption Processes

In addition to the charge stored within the boundary layer, adsorbed species on the electrode surface can contribute to the total double layer capacitance.

Analogously to the electrolyte, the steric size of adsorbed species is modelled as a surface partial molar area a_α, where the effective molar area is modelled as

$$a_\alpha = \tilde{a}_\alpha + \underset{s}{\kappa_\alpha} a_0, \tag{22}$$

where $\tilde{a}_\alpha$ is the molar area of the central ion, $\underset{s}{\kappa_\alpha}$ is the surface solvation shell of species α and

a_0 is the surface molar area of the solvent molecule.

An important characteristic of the electrode surface is the surface density of adsorption sites for the electrolyte species. The density of the metal ions is described by a molar area a_M. Furthermore, each metal ion site is assumed to provide ω_M adsorption sites for the species.

As derived in [12], the resulting equilibrium molar fractions of adsorbed species is given by

$$\underset{s}{y_\alpha} = y_{E,\alpha} \exp\left(-\Delta g^{\mathrm{ads}} f - z_\alpha f \Delta\phi + \frac{a_\alpha}{RT}\Delta\gamma\right), \tag{23}$$

where Δg^{ads} denotes the adsorption energy and $\Delta\gamma$ is the difference of the surface tension with respect to a reference state corresponding to a surface containing no adsorbed species. Analogously, the molar fraction of free sites containing no adsorbed species is given by

$$\underset{s}{y_v} = \exp\left(\frac{a_M}{\omega_M RT}\Delta\gamma\right). \tag{24}$$

For a given potential difference $\Delta\phi$, the surface tension difference $\Delta\gamma$ is then determined implicitly by the constraint

$$\underset{s}{y_v} + \sum_\alpha \underset{s}{y_\alpha} = 1. \tag{25}$$

The surface coverage of species α can then be evaluated as

$$\theta_\alpha = \underset{s}{y_\alpha} a_\alpha \underset{s}{c}, \tag{26}$$

where

$$\underset{s}{c} = \left(\sum_\alpha a_\alpha \underset{s}{y_\alpha} + a_v \underset{s}{y_v}\right)^{-1} \tag{27}$$

is the total (molar) surface concentration.

As shown in [12], the capacitance due to adsorbed species is related to the surface tension by

$$\underset{s}{C} = -\left.\frac{\partial^2 \Delta\gamma}{\partial\phi^2}\right|_{\Delta\phi}. \tag{28}$$

Finally, the total double layer capacitance is determined by the sum of the capacitance of the boundary layer and the surface capacitance as

$$C = C_{\mathrm{BL}} + \underset{s}{C}. \tag{29}$$

2.6 Bayesian Inference of Model Parameters

A full parameterization of the reduced interface model requires knowledge of processes and properties at the atomistic scale, such as adsorption energies or solvation shell numbers. While these parameters cannot be inferred by the reduced model considered here, it is often possible to define meaningful a-priori ranges based on physical insight for these parameters. As such, a statistical approach is adopted, where most model parameters are described by a statistical distribution, allowing for the incorporation of the inherent uncertainties in the modelling parameters. Here we consider these parameters to be normally and independently distributed.

We use Bayesian inference methods to update the probability distributions of the prior parameter estimates by incorporating additional atomistic KMC results or experimental measurements. The Bayesian framework naturally incorporates the uncertainties of both the prior distributions and the data used to update the model parameters.

Let θ denote a vector of model parameters and $p(\theta)$, the corresponding a-priori probability density based on the initial parameter estimates. In Bayesian inference, the a-posteriori distribution of the model parameters is determined by Bayes' theorem

$$p(\theta|\mathbf{X}) = \frac{p(\mathbf{X}|\theta)p(\theta)}{p(\mathbf{X})} \propto p(\mathbf{X}|\theta)p(\theta), \tag{30}$$

where $p(\theta|\mathbf{X})$ is the posterior probability of the parameters θ for a given vector of data samples $\mathbf{X}$, which could e.g. contain KMC simulations results. Furthermore, $p(\mathbf{X}|\theta)$ is the likelihood of observing the data $\mathbf{X}$ for the given parameter values θ. Finally, the probability density $p(\mathbf{X})$ is called the marginal likelihood and plays the role of a normalizing factor.

Additionally, the MAP (maximum a-posteriori probability) estimate can be evaluated by solving the optimization problem

$$\hat{\theta}_{\mathrm{MAP}} = \arg\max_{\theta} p(\theta|\mathbf{X}) = \arg\max_{\theta} p(\mathbf{X}|\theta)p(\theta), \tag{31}$$

such that the MAP estimate corresponds to the mode of the posterior distribution in Eq. (30).

In Figure 2 we show the proposed work flow of the parameter estimation, and the interrelations with the data provided by WP2 and WP3.

We implemented the reduced interface model in *Julia*, which is an emerging dynamic high-level and efficient programming language specifically targeting the demands of scientific software. We use the open-source Julia library *Turing.jl*, which provides a system for efficiently building MCMC algorithms using probabilistic programming, see [10].

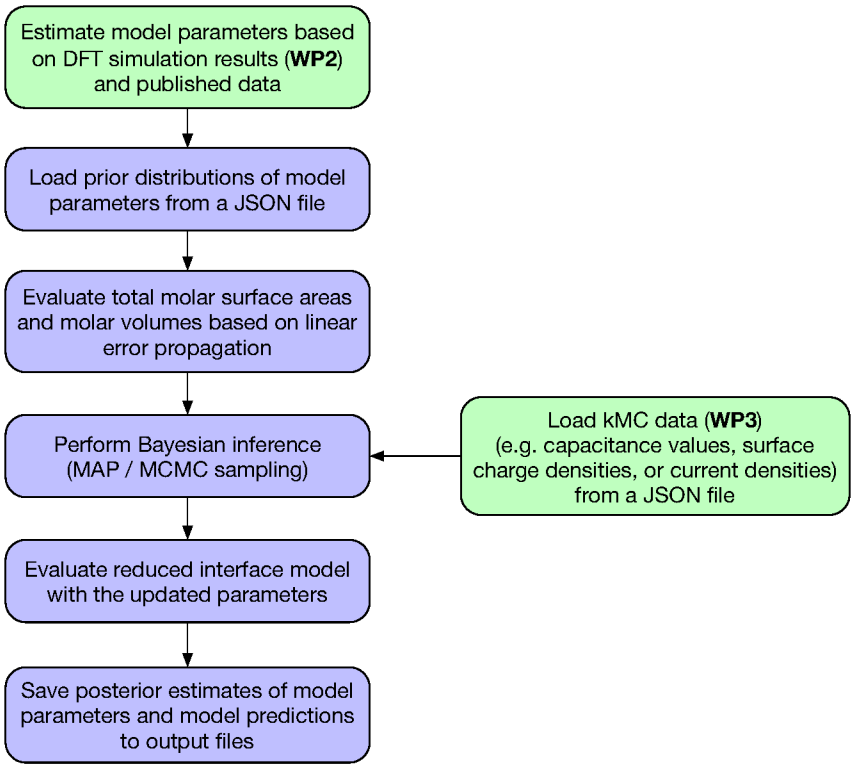

Figure 2: Parameter estimation and model prediction work flow.

2.7 Model Extensions

In the DGLM-theory, the susceptibility throughout the double layer is assumed to be constant. However, in reality the susceptibility of the electrolyte can depend both on the strength of the electrical field and the ion concentrations. A possible extension to concentration-dependent susceptibility values has been discussed in [3, 12], where the authors remark that a generalization to a concentration-dependent susceptibility leads to a significantly more complex Poisson-momentum system.

Here we considered quasi-static processes, where the double layer structure is determined by its equilibrium state. For fast varying electrode processes, such as high-frequency modulations of the electrostatic potential or rapidly changing bulk concentrations, a time-resolved solution to the coupled modified PNP and momentum system would be required in the general case.

3 Results

In this section we present verification studies of the implemented models and parameter estimation methods, as well as applications to the organic electrolytes methyl-viologen (MV) and 4-OH-TEMPO (T) that are used in all-organic redox flow battery applications [11, 15].

3.1 Application to an Electroplating Process

To study the validity of the parameter estimation method when applied to electrochemical reactions, we consider the application of the generalized Butler-Volmer equation to an electroplating process that has been investigated in [4]. In this example the electrolyte consists of water as the solvent, the anions SO_4^{2-} and cations Cu^{2+}. Here we consider the electrochemical reduction reaction of the cupric cations at the cathode according to

$$\mathrm{Cu}^{2+} + e^- \rightleftharpoons \mathrm{Cu}^{+}, \tag{32}$$

where the reduced species are integrated on the electrode surface. Specializing the general extended Butler-Volmer type equation to this process yields the Faradaic current density [4]

$$j_e = z_{\mathrm{ox}} F \underset{s}{R_0} \left(\left(\frac{c_{\mathrm{ox}}}{\bar{c}_{\mathrm{ox}}} \right)^{\underset{s}{\beta}} e^{-\underset{s}{\beta} \underset{s}{A} z_{\mathrm{ox}} f \eta_s} - \left(\frac{\bar{c}_{\mathrm{ox}}}{c_{\mathrm{ox}}} \right)^{1-\underset{s}{\beta}} e^{(1-\underset{s}{\beta}) \underset{s}{A} z_{\mathrm{ox}} f \eta_s} \right), \tag{33}$$

where $\underset{s}{R_0}, \underset{s}{\beta}, \underset{s}{A}$ denote the unknown phenomenological coefficients of the extended Butler-Volmer equation and $\{c_{\mathrm{ox}}, c_{\mathrm{red}}\}$ denote the molar bulk concentrations of the oxidized and reduced copper ions evaluated just outside the double layer structure. The corresponding equilibrium molar concentrations are given by $\bar{c}_{\mathrm{ox}}, \bar{c}_{\mathrm{red}}$.

Based on the results of a fully spatially resolved solution of the bulk ion concentrations shown in [4] we set in this example the concentration of c_{ox} and $\bar{c}_{\mathrm{ox}}$ at the cathode to

$$c_{\mathrm{ox}} = \bar{c}_{\mathrm{ox}} - 0.005\, j_e \ \mathrm{mol\,L^{-1}}, \quad \bar{c}_{\mathrm{ox}} = 0.5 \ \mathrm{mol\,L^{-1}}. \tag{34}$$

Based on measured properties of the chemical system [12], the exact values are estimated as $\underset{s}{A} = 1.0$, $\underset{s}{\beta} = 0.25$, $\underset{s}{R_0} = 1.75 \cdot 10^{-5}$. Using these parameters, a set of reference values, relating the Faradaic current j_e to the overpotential η_s, are evaluated as shown in Fig. 3. The prior distributions of these parameters are assumed to be normally distributed according to

$$\underset{s}{A} \sim \mathcal{N}(1,1), \quad \underset{s}{\beta} \sim \mathcal{N}(1/2, 1/2), \quad \underset{s}{R_0} \sim \mathcal{N}(10^{-5}, 10^{-5}), \tag{35}$$

where $\mathcal{N}(\mu, \sigma)$ denotes a normal distribution with mean μ and standard deviation σ. The large

uncertainty in these parameters is reflected in choosing the standard deviations to be the same value as the corresponding mean value.

We assume the measured current density of the reference values displayed in Fig. 3 to be normally distributed with a standard deviation of 10% of its mean value. The resulting maximum a-posteriori probability (MAP) of the model parameters then matches the mean values of the reference values over 2 significant digits and the resulting model evaluation based on the MAP estimate is in excellent agreement with the reference values as shown in Fig. 3.

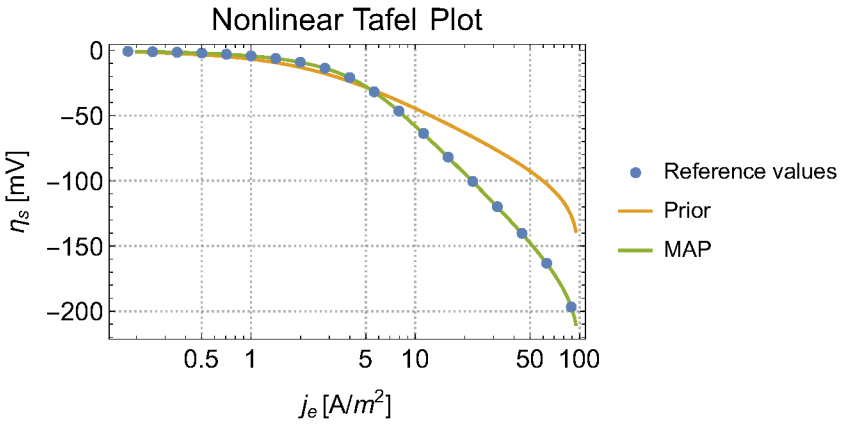

Figure 3: Tafel plot of the exact reference values, together with the model predictions based on the prior parameter modes and the MAP estimate.

In addition to the mode of the a-posteriori distribution, we estimate the full a-posteriori distributions of the model parameters using the MCMC No-U-Turn-sampler (NUTS) provided by the *Turing.jl* package with a target acceptance ratio of $p_a = 0.65$ and $N = 20000$ samples. Approximating the a-posteriori distributions in terms of Normal distributions yields

$$\underset{s}{A} \sim \mathcal{N}(1.00, 0.083), \quad \underset{s}{\beta} \sim \mathcal{N}(0.25, 0.018), \quad \underset{s}{R_0} \sim \mathcal{N}(1.76 \cdot 10^{-5}, 0.12 \cdot 10^{-5}), \tag{36}$$

which shows that the reference values allow for a significant reduction of the uncertainty in the model parameters. In this case, the remaining uncertainty in the estimated parameters reflects the assumed uncertainty in the reference values.

3.2 Verification Studies of the Double Layer Properties

In this section we perform several studies of the implemented model to verify the correctness with published results in [12]. Furthermore, we show another application of the MAP estimator to improve the model prediction with respect to experimentally measured capacitance values.

3.2.1 A Symmetric Electrolyte Example

A simple symmetric electrolyte consisting of water molecules H_2O, a cationic species C^+, and an anionic species A^- was considered in [6]. Due to charge neutrality in the electrolyte bulk, the molar species concentrations must satisfy $c^b_{C^+} = c^b_{A^-}$. For simplicity, the molar volume of all species is assumed to be equal $\nu_{H_2O} = \nu_{C^+} = \nu_{A^-} \approx 1.805 \times 10^{-5}$. Furthermore, species adsorption is neglected in this case and the electrolyte susceptibility is set to $\chi_E = 80$.

To verify the agreement of the current study with the published results, we show in Fig. 4 the charge stored in the double layer structure as a function of the potential difference for different molar concentrations of the ionic species in the electrolyte bulk.

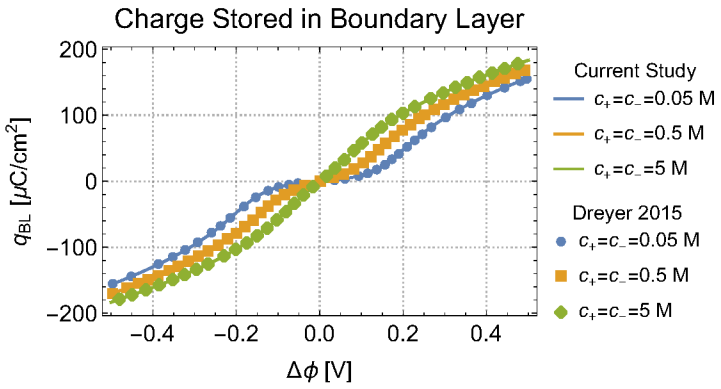

Figure 4: Verification of the charge stored in the boundary layer.

3.2.2 Applications to Different Electrolytes on a Silver Surface

In this section we apply the reduced electrochemical interface model to a silver surface Ag110, which is characterized by a molar area per metal ion of $a_M = 7.1233 \times 10^4$ and the number of adsorption sites per metal ion is assumed as $\omega_M = 1$. Here the electrolyte susceptibility value is set to $\chi_E = 25$. The adsorption energies of protons and hydroxide ions are modelled as

$$\Delta\tilde{g}^{ads}_{H^+} = \Delta\tilde{g}^{ads}_{OH^-} = \frac{1}{2}\left(\Delta g^{ads}_{H_2O} + \underset{s}{\Delta} g^{D}_{H_2O} - \Delta g^{D}_{H_2O}\right), \tag{37}$$

where $\underset{s}{\Delta} g^{D}_{H_2O}, \Delta g^{D}_{H_2O}$ are the dissociation energies of water on the electrode surface and the electrolyte, respectively. Their values are assumed to be $\underset{s}{\Delta} g^{D}_{H_2O} = 0.05\,\mathrm{eV}$ and $\Delta g^{D}_{H_2O} = 1.034\,\mathrm{eV}$.

The bulk molar concentrations of the hydrogen and hydroxide ions in a neutral solution with $pH = 7$ are given by $c_{H^+} = c_{OH^-} = 1 \times 10^{-7}\,\mathrm{mol\,L^{-1}}$.

In Table 1 we summarize the most significant model parameters concerning the properties of electrolyte species, such as their adsorption energy, solvation shell or size in terms of molar volumes and molar areas on the electrode surface.

Species	κ [−]	κ_s [−]	$\tilde{\nu}$ [m^3 mol^{-1}]	$\tilde{a}$ [m^2 mol^{-1}]	$\Delta\tilde{g}^{\text{ads}}$ [eV]
H_2O	0	0	1.7973×10^{-5}	7.0052×10^{4}	-0.08
H^+	45	25	1.7973×10^{-5}	7.0052×10^{4}	-0.53
OH^-	45	25	1.7973×10^{-5}	7.0052×10^{4}	-0.53
Na^+	45	25	1.7973×10^{-5}	7.0052×10^{4}	∞
F^-	45	8	1.7973×10^{-5}	7.0052×10^{4}	-0.16
$PF6^-$	45	25	1.7973×10^{-5}	7.0052×10^{4}	∞
K^+	45	25	1.7973×10^{-5}	7.0052×10^{4}	∞

Table 1: Model species parameters as specified in [12].

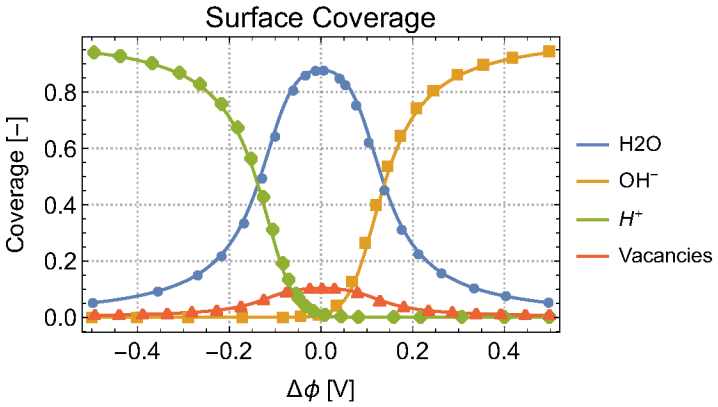

Figure 5: Predicted surface coverage, where the symbols correspond to report values in [12] and full lines to the current study.

In Figure 5, the predicted surface coverage with H^+ and OH^- species is shown as a function of the electrostatic potential difference across the double layer, where the symbols denote the reported values in [12]. This simple illustration shows that even species with very small bulk concentrations can cover the electrode surface area to a significant degree.

The surface tension is intimately linked to the adsorption of species and the resulting surface capacitance. In Fig. 6 we verify the prediction of the surface tension difference $\Delta\gamma$ for an electrolyte system consisting of water and the four ionic species H^+, OH^-, PF_6^-, and K^+.

In Figure 7 the predicted total capacitance is displayed for two different concentrations of the KPF_6 salt. The capacitance curve follows a characteristic camel shape, where the capacitance attains two maxima.

As a last verification example, we considered an electrolyte containing water as the solvent and the four ionic species H^+, OH^-, F^- and Na^+. Compared to the KPF_6 electrolyte, the surface solvation shells of F^- and Na^+ are assumed to be different. Furthermore, F^- can adsorb to the electrode surface, see Table 1. As a result, the capacitance curve, as shown in Fig. 8, is strongly asymmetric. In the same figure we show a comparison with experimental results

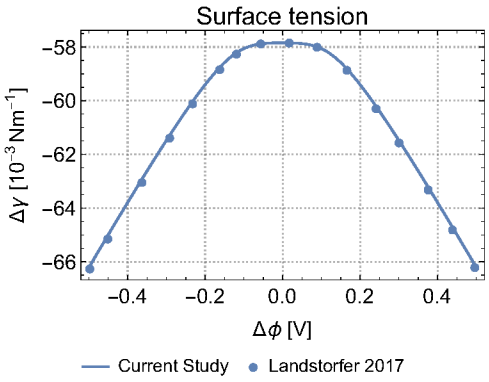

Figure 6: Verification of the predicted surface tension as a function of the potential difference.

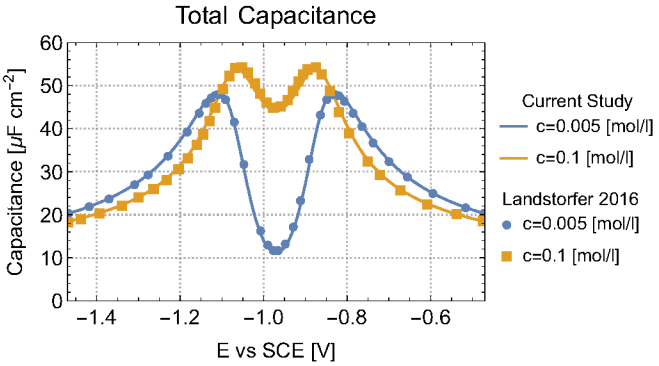

Figure 7: Predicted total capacitance as a function of the half-cell potential.

reprinted in [12], which show a remarkable agreement, considering the simplicity of the model proposed in [12].

Since most model parameters used in the prediction of the total capacitance are affected by uncertainties, we can try to improve the estimation based on the available measurement data. In this example we consider the electrolyte susceptibility, as well as the molar areas, molar volumes, and adsorption energies of the $\{\mathrm{Na}^+, \mathrm{F}^-\}$ species to be unknown by specifying large standard deviations. In Figure 9 we show the model prediction based on the prior model parameters and the MAP estimates, together with the measurements. Clearly, the MAP estimate provides in this case a significantly improved agreement with the measurements.

3.3 Application to Organic Electrolytes at a Graphene Electrode

In this section we show the application of the model to two organic electrolytes at a graphene electrode. In Table 2 we summarize the used model parameters, which are based on literature values, as well as DFT calculations provided by WP2. If not stated otherwise, the susceptibility of the electrolyte is $\chi_E = 25$, the solvation number of the ionic species is $\kappa = 15$ and the surface

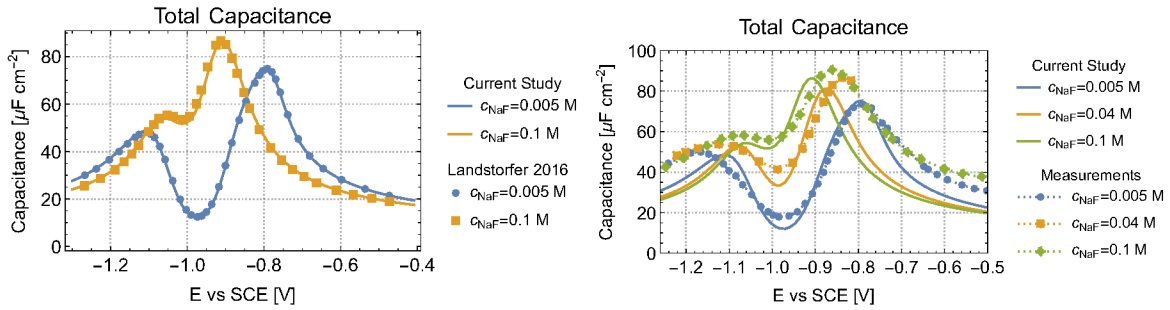

Figure 8: Verification of the total capacitance (left) and validation against experimental measurements (right).

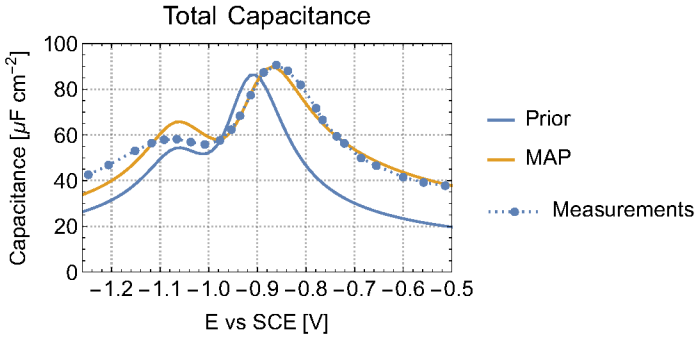

Figure 9: Model evaluation based on the mode of the prior parameters and the MAP estimate, together with the experimental measurements for $c_{\mathrm{NaF}} = 0.1\,\mathrm{M}$.

solvation number is $\kappa_s = 5$.

3.3.1 Methyl-Viologen

In RFB systems using methyl-viologen, often no supporting electrolyte is being used, see e.g. [16]. In this case, the electrolyte consists of $\mathrm{H_2O}$ as the solvent, the reduced and oxidized states $\{\mathrm{MV}^+, \mathrm{MV}^{2+}\}$ of MV, as well as chloride ions Cl^-. In Fig. 10 we show the capacitance for various ion concentrations and concentration ratios of the oxidized and reduced forms, corresponding to different state of charge values of the battery. Similar to the NaF electrolyte shown above, the capacitance curve is strongly asymmetric with a camel shape at low concentration that converges to a single bell-shaped curve at high concentrations of the electroactive species.

In Fig. 11 we show the influence of the chosen electrolyte susceptibility and solvation shell numbers on the total capacitance. While the susceptibility shifts the capacitance by a constant, varying solvation shell numbers affect both the overall capacitance, the capacitance peak and the peak location.

As shown in Fig. 12, the surface covereage is dominated either by H^+ ions or Cl^-, depending on the potential difference.

Species	κ [−]	$\underset{s}{\kappa}$ [−]	$\tilde{\nu}$ [$m^3\,mol^{-1}$]	$\tilde{a}$ [$m^2\,mol^{-1}$]	$\Delta\tilde{g}^{ads}$ [eV]
H_2O	0	0	1.8×10^{-5}	7.0×10^{4}	−0.08
H^+	κ	$\underset{s}{\kappa}$	1.8×10^{-5}	7.0×10^{4}	−0.53
OH^-	κ	$\underset{s}{\kappa}$	5.9×10^{-6}	3.3×10^{4}	−0.53
Na^+	κ	$\underset{s}{\kappa}$	4.0×10^{-6}	2.6×10^{4}	−0.67
Cl^-	κ	$\underset{s}{\kappa}$	1.1×10^{-5}	5.1×10^{4}	−0.16
MV^+	κ	$\underset{s}{\kappa}$	1.6×10^{-4}	3.0×10^{5}	−1.26
MV^{2+}	κ	$\underset{s}{\kappa}$	1.6×10^{-4}	3.0×10^{5}	−1.14
T	0	0	1.3×10^{-4}	2.6×10^{5}	−0.74
T^+	κ	$\underset{s}{\kappa}$	1.3×10^{-4}	2.6×10^{5}	−1.37

Table 2: Model parameters of the electrolyte species.

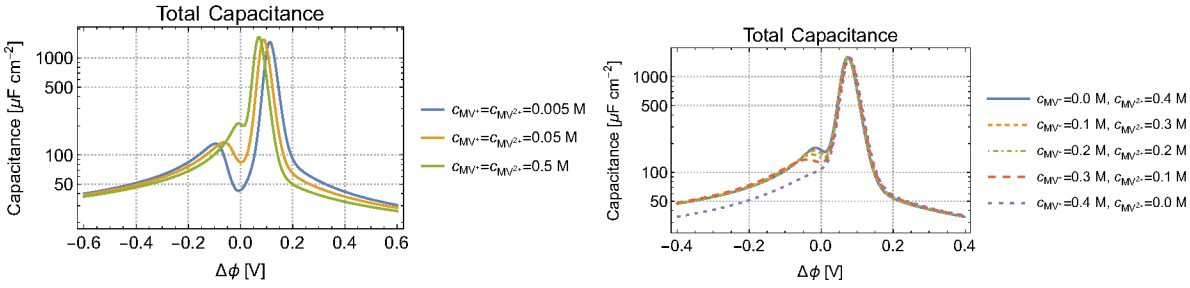

Figure 10: Total capacitance for various ion concentrations at fixed composition (left) and different compositions (right).

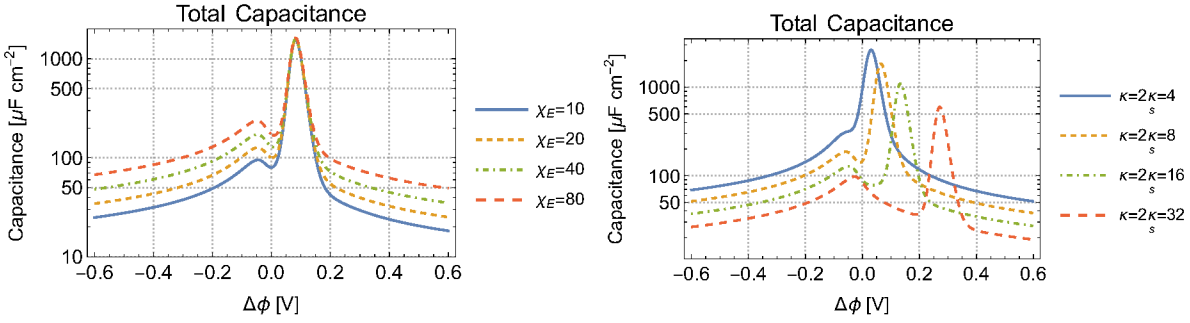

Figure 11: Total capacitance for varying susceptibilites (left) and solvation shell numbers (right).

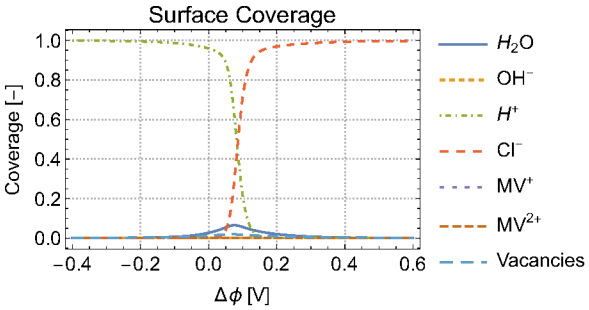

Figure 12: Surface coverage vs the electrostatic potential difference.

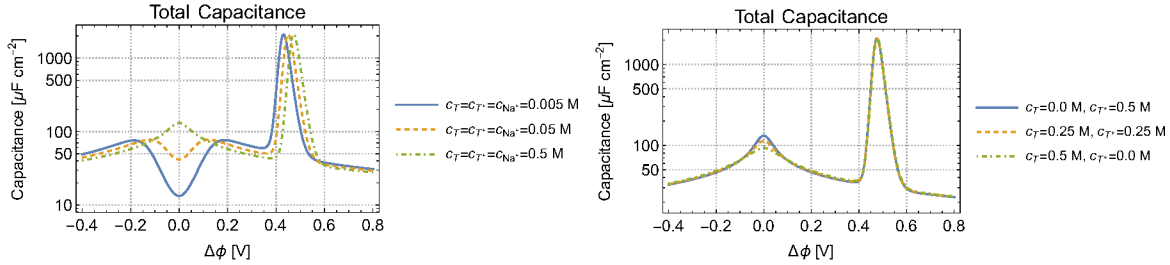

Figure 13: Total capacitance for varying total ion concentrations (left) and different compositions (right), where the sodium concentration is fixed to $c_{\mathrm{Na}^+} = 0.4\,\mathrm{M}$.

3.3.2 4-OH-TEMPO

Finally, we consider the application to an electrolyte containing 4-OH-TEMPO (T) as the electroactive material. In this case, the electrolyte contains $\mathrm{H_2O}$, T, T^+, and $\mathrm{Na}^+, \mathrm{Cl}^-$ as the supporting electrolyte species. In Fig. 12 we show the predicted surface coverage as a function of the potential difference. In Fig. 13 we report the predicted capacitance as function of the electrolyte concentrations and varying ratios of the reduced and oxidized forms of the electroactive species. Similar the MV electrolyte shown before, a large capacitance peak is predicted, which is only marginally affected by differences in the electrolyte composition, whereas a smaller capacitance peak forms at $\Delta\phi = 0\,\mathrm{V}$, which strongly depends on the electrolyte concentration.

3.4 Discussion

The applications to the MV and 4-OH-TEMPO electrolytes show first model predictions with model parameters determined by DFT calculations (WP2), literature values, and educated guesses [12]. As such, the predicted surface coverage and capacitance values can be expected to be strongly affected by the uncertainties in the model parameters, as the parameter studies with varying susceptibility values and solvation shell numbers have illustrated.

The parameter identification methods based on Bayesian inference allow for a very natural work flow, where the initial model parameterization is improved upon the incorporation of addi-

tional measurements or atomistic simulation results. Furthermore, as the Bayesian inference also allows estimating the uncertainties of the updated model parameters, sensitivity studies can be performed not only on the initial parameterization, but also on the updated parameterization.

4 Conclusions

We presented the application of a reduced model for the electrochemical interface to different electrolyte systems, including the organic methyl-viologen and 4-OH-TEMPO chemistries. The reduced model allows for a thermodynamically consistent description of important interface processes, such as adsorption of electrolyte species to the electrode surface, charging of the double layer, and (electro-) chemical reactions.

The applicability of the reduced electrochemical interface model requires a scale separation between the Debye length and the characteristic length scale of the electrolyte flow (e.g. in a porous electrode), which is fulfilled in RFB applications under typical operating conditions. The assumption of a quasi-equilibrium state of the electrochemical double layer limits the application of the model to slowly changing boundary conditions, see [4, 6]. However, the quasi-equilibrium assumption can be expected to hold in typical charge-discharge cycling experiments, where both the bulk concentrations and the cell voltage change slowly in time.

In contrast to atomistic models, such as KMC and DFT, the reduced electrochemical interface model only captures a small subset of the physico-chemical effects within the double layer. Therefore, some model parameters, such as the electrolyte susceptiblity, which is known to vary spatially throughout the double layer structure, can be regarded as effective parameters, which have be tuned to improve the model accuracy with respect to experimental measurements and atomistic simulations.

We demonstrated the applicability of the parameter estimation method for two example problems. As a next step we want to apply the proposed work flow on KMC data produced by WP3 for the estimation of the model parameters for different organic electrolyte systems. The resulting improved parameterization of the reduced electrochemical interface model can then be used to investigate the interface properties under different operating conditions and carry out sensitivity analyses. Furthermore, the reduced interface will serve as an efficient, thermodynamics-based boundary condition in pore-scale models that we develop as part of Task 4.3.

Acknowledgments

The authors gratefully appreciate the financial support from the European Union's Horizon 2020 research and innovation programme under Grant Agreement no. 875489 (SONAR).

Table of Symbols

Symbol	Description	Unit
a_α	Surface molar area of adsorbed species α	$\mathrm{m^2\,mol^{-1}}$
$\underset{s}{A}$	Phenomenological coefficient in the extended Butler-Volmer equation	–
c	Total molar concentration	$\mathrm{mol\,L^{-1}}$
c_α	Molar concentration of species α	$\mathrm{mol\,L^{-1}}$
j_e	Electric current density	$\mathrm{A\,m^{-2}}$
f	Inverse thermal voltage ($f = F/(RT)$)	$\mathrm{V^{-1}}$
F	Faraday constant	$\mathrm{C\,mol^{-1}}$
q_{BL}	Charge stored in the boundary layer	C
R	Ideal (molar) gas constant	$\mathrm{J\,mol^{-1}\,K^{-1}}$
$\underset{s}{R}, \underset{s}{R_0}$	Reaction rate	$\mathrm{mol\,s^{-1}\,m^{-2}}$
T	Temperature	K
y_α	Molar fraction of species α	–
$\underset{s}{y_v}$	Molar fraction of vacant sites on the electrode surface	–
Greek symbols	**Description**	**Unit**
$\underset{s}{\beta}$	Phenomenological coefficient (corresponding to the symmetry coefficient)	–
η_s	Overpotential	V
γ	Surface tension	$\mathrm{J\,m^{-2}}$
κ_α	Solvation number of species α	–
μ_α	Chemical potential of species α	$\mathrm{J\,kg^{-1}}$
ν_α	Partial molar volume of species α	$\mathrm{m^3\,mol^{-1}}$
Subscripts	**Description**	**Unit**
α	Refers to species α	–
s	Refers to species located on the electrode surface	–
E	Refers to the electrolyte bulk domain	–
M	Refers to the metal bulk domain	–

Table 3: List of symbols used in the report.

References

[1] J.J. Bikerman. “XXXIX. Structure and Capacity of Electrical Double Layer”. In: *The London, Edinburgh, and Dublin Philosophical Magazine and Journal of Science* 33.220 (May 1942), pp. 384–397. ISSN: 1941-5982, 1941-5990. DOI: 10.1080/14786444208520813 (cit. on p. 3).

[2] Itamar Borukhov et al. “Steric Effects in Electrolytes: A Modified Poisson-Boltzmann Equation”. In: *Phys. Rev. Lett.* 79.3 (July 21, 1997), pp. 435–438. ISSN: 0031-9007, 1079-7114. DOI: 10.1103/PhysRevLett.79.435 (cit. on p. 3).

[3] W. Dreyer et al. “New Insights on the Interfacial Tension of Electrochemical Interfaces and the Lippmann Equation”. In: *Eur. J. Appl. Math* 29.4 (Aug. 2018), pp. 708–753. ISSN: 0956-7925, 1469-4425. DOI: 10.1017/S0956792517000341 (cit. on p. 11).

[4] Wolfgang Dreyer et al. “A New Perspective on the Electron Transfer: Recovering the Butler–Volmer Equation in Non-Equilibrium Thermodynamics”. In: *Phys. Chem. Chem. Phys.* 18.36 (2016), pp. 24966–24983. ISSN: 1463-9076, 1463-9084. DOI: 10.1039/C6CP04142F (cit. on pp. 3, 5, 6, 12, 20).

[5] Wolfgang Dreyer et al. “Bulk-Surface Electrothermodynamics and Applications to Electrochemistry”. In: *Entropy* 20.12 (Dec. 6, 2018), p. 939. ISSN: 1099-4300. DOI: 10.3390/e20120939 (cit. on p. 3).

[6] Wolfgang Dreyer et al. “Modeling of Electrochemical Double Layers in Thermodynamic Non-Equilibrium”. In: *Phys. Chem. Chem. Phys.* 17.40 (2015), pp. 27176–27194. ISSN: 1463-9076, 1463-9084. DOI: 10.1039/C5CP03836G (cit. on pp. 3–5, 14, 20).

[7] Wolfgang Dreyer et al. “Overcoming the Shortcomings of the Nernst–Planck Model”. In: *Phys. Chem. Chem. Phys.* 15.19 (2013), p. 7075. ISSN: 1463-9076, 1463-9084. DOI: 10.1039/c3cp44390f (cit. on p. 4).

[8] Rocco Peter Fornari and Piotr de Silva. “A Computational Protocol Combining DFT and Cheminformatics for Prediction of pH-Dependent Redox Potentials”. In: *Molecules* 26.13 (June 29, 2021), p. 3978. ISSN: 1420-3049. DOI: 10.3390/molecules26133978 (cit. on p. 3).

[9] Antoni Forner-Cuenca et al. “Exploring the Role of Electrode Microstructure on the Performance of Non-Aqueous Redox Flow Batteries”. In: *J. Electrochem. Soc.* 166.10 (2019), A2230–A2241. ISSN: 0013-4651, 1945-7111. DOI: 10.1149/2.0611910jes (cit. on p. 4).

[10] Hong Ge et al. “Turing: A Language for Flexible Probabilistic Inference”. In: *Proceedings of the Twenty-First International Conference on Artificial Intelligence and Statistics*. Proceedings of Machine Learning Research. PMLR, 2018, pp. 1682–1690 (cit. on p. 10).

[11] Tobias Janoschka et al. “An Aqueous Redox-Flow Battery with High Capacity and Power: The TEMPTMA/MV System”. In: *Angew. Chem. Int. Ed.* 55.46 (Nov. 7, 2016), pp. 14427–14430. ISSN: 14337851. DOI: 10.1002/anie.201606472 (cit. on p. 12).

[12] M. Landstorfer et al. “Theory and Structure of the Metal-Electrolyte Interface Incorporating Adsorption and Solvation Effects”. In: *Electrochimica Acta* 201 (May 2016), pp. 187–219. ISSN: 00134686. DOI: 10.1016/j.electacta.2016.03.013 (cit. on pp. 3, 7–9, 11–13, 15, 16, 19).

[13] Jin Yong Lee. “Ionic Size Effect on the Double Layer Properties: A Modified Poisson-Boltzmann Theory”. In: *Bull. Korean Chem. Soc.* 31.9 (Sept. 20, 2010), pp. 2553–2556. DOI: 10.5012/BKCS.2010.31.9.2553 (cit. on p. 3).

[14] Jinn-Liang Liu and Bob Eisenberg. “Molecular Mean-Field Theory of Ionic Solutions: A Poisson-Nernst-Planck-Bikerman Model”. In: *Entropy* 22.5 (May 14, 2020), p. 550. ISSN: 1099-4300. DOI: 10.3390/e22050550 (cit. on p. 3).

[15] Tianbiao Liu et al. “A Total Organic Aqueous Redox Flow Battery Employing a Low Cost and Sustainable Methyl Viologen Anolyte and 4-HO-TEMPO Catholyte”. In: *Adv. Energy Mater.* 6.3 (Feb. 2016), p. 1501449. ISSN: 16146832. DOI: 10.1002/aenm.201501449 (cit. on p. 12).

[16] Gaël Mourouga et al. “Physics-Based 0D-U-I-SoC Cell Performance Model for Aqueous Organic Redox Flow Batteries”. In: *Electrochem. Acta* (2022). DOI: 10.1016/j.electacta.2022.140185 (cit. on p. 17).

[17] Christopher W. Outhwaite and Lutful B. Bhuiyan. “An Improved Modified Poisson–Boltzmann Equation in Electric-Double-Layer Theory”. In: *J. Chem. Soc., Faraday Trans. 2* 79.5 (1983), pp. 707–718. ISSN: 0300-9238. DOI: 10.1039/F29837900707 (cit. on p. 3).

[18] Matias A. Quiroga and Alejandro A. Franco. “A Multi-Paradigm Computational Model of Materials Electrochemical Reactivity for Energy Conversion and Storage”. In: *J. Electrochem. Soc.* 162.7 (2015), E73–E83. ISSN: 0013-4651, 1945-7111. DOI: 10.1149/2.1011506jes (cit. on p. 3).

[19] Kathleen Schwarz and Ravishankar Sundararaman. “The Electrochemical Interface in First-Principles Calculations”. In: *Surface Science Reports* 75.2 (May 2020), p. 100492. ISSN: 01675729. DOI: 10.1016/j.surfrep.2020.100492 (cit. on p. 3).

[20] Stefan Woelki and Hans-Helmut Kohler. “A Modified Poisson-Boltzmann Equation I. Basic Relations”. In: *Chem. Phys.* (2000), p. 9 (cit. on p. 3).